Extreme Mechanics Letters 61 (2023) 101986

Contents lists available at ScienceDirect

Extreme Mechanics Letters

journal homepage: www.elsevier.com/locate/eml

Resolving stress state at crack tip to elucidate nature of elastomeric fracture

Zehao Fan, Shi-Qing Wang *

School of Polymer Science and Polymer Engineering, University of Akron, Akron, OH 44325, United States of America

ARTICLE INFO

Article history:
Received 5 December 2022
Received in revised form 1 February 2023
Accepted 21 February 2023
Available online 27 February 2023

Keywords:
Elastomeric fracture
Polymer physics
Linear elastic fracture mechanics
Photoelasticity

ABSTRACT

Based on spatial–temporal resolved measurements of the stress field at crack tip using polarized optical microscopy (*str*-POM), we develop an stress analysis approach to elastomeric fracture. Specifically, *str*-POM measurements reveal emerging phenomenology in three distinct ways. First, there emerges a stress saturation zone (SSZ) whose dimension r_{ss} is independent of the stress intensity factor K. This SSZ arises from the fact that the precut suffers natural blunting during cut making. Because of the finite radius of the cut tip, the tip stress σ_{tip} is well defined and experimentally accessible, i.e., can be determined within the spatial resolution of *str*-POM. At the onset of fracture, the tip stress is interpreted to reach inherent material strength $\sigma_{F(inh)}$, i.e., $\sigma_{tip(F)} = \sigma_{F(inh)}$. Second, elastomeric fracture in pure shear is shown by the *str*-POM observations to involve the same physics: Fracture occurs when the tip stress approaches the inherent strength. Rivlin–Thomas expression for toughness $G_c = w_c h_0$ follows because the stress buildup at the cut tip explicitly scales with specimen height h_0, i.e., $K_{ps} = \sigma\sqrt{h_0}$, as expected. Third, the *str*-POM observations reveal how elastomeric fracture occurs at a common K_c independent of specimen thickness. At a given load there is weaker stress buildup for a thicker specimen due to greater stress saturation at cut tip, and fracture is observed to occur at lower tip stress for a thicker specimen.

1. Introduction

The fracture behavior of solids is a most important topic in materials science and engineering. Soft materials also undergo fracture [1,2]. After a hundred years [3] of extensive research [4] fracture mechanics has become a more mature subject, guiding research on fracture of modern materials including polymers. Effects of large cracks on the strength of brittle polymers including plastics and elastomers can indeed be characterized by toughness G_c, also known as the critical energy release rate [4,5]. For both glassy polymers [6,7] and crosslinked rubbers [8], since G_c has been found to be hundreds or thousands times greater than the surface fracture energy Γ, within fracture mechanics we can no longer *a priori* prescribe the magnitude of G_c. While any microscopic modeling of G_c can be regarded as a theoretical inquiry to search for the fracture mechanism, we often fail to find the calculated G_c in agreement with experiment. Related to these issues is whether polymers are flaw intolerant, i.e., whether brittle fracture of polymers without intentional through-cut is due to presence of intrinsic flaws or defects, as implied in the literature [5].

Since the beginning of linear-elastic fracture mechanics (LEFM) [9–11], there has been the recognition that "fracture is governed by the local stress and deformation conditions around the crack tip" [12]. However, the difficulty of the perceived stress singularity [10,13] makes it convenient to adopt the Griffith [3]-Irwin [14] energy balance argument. Thus, fracture behavior has ever since been conveniently characterized in terms of global conditions, i.e., through the measurement of G_c based on its operational definition ($G_c \sim \sigma_c^2 a/E$) for a given cut size a at critical far-field load σ_c for fracture. For elastomers, Rivlin and Thomas extended [8] LEFM to propose a pure-shear protocol for measurement of the toughness G_c.

Separately, according to textbooks [4,5] the critical stress intensity factor K_c changes with specimen thickness for certain materials (e.g., metals). As the state of stress changes from plane stress (thin) to plane strain (thick), K_c tends to decrease [15]. This thickness dependence of K_c acquired a particularly convenient interpretation in the energy approach: there is less plastic dissipation under plane strain, with lower G_c implying lower K_c. However, we note that the literature on fracture of rubbers shows [16] independence of fracture toughness on specimen thickness. Moreover, toughness of rubber has been observed to increase with crack propagation speed, examined either in terms of tensile extension of precut specimens [16,17] or tearing

* Corresponding author.
E-mail address: swang@uakron.edu (S.-Q. Wang).

https://doi.org/10.1016/j.eml.2023.101986
2352-4316/

[18,19]. This increase of toughness with speed has been interpreted in terms of linear viscoelastic characteristics [19–23], first proposed by Mullins [24,25].

Based on fracture behavior of two elastomers, in this work we explore and establish that elastomeric fracture can be characterized in terms of the crack tip stress exceeding inherent strength. Specifically, using recently adopted spatial–temporal resolved polarized-optical microscopy (*str*-POM) [26] we address the following questions to demonstrate the merit of quantifying local processes at crack tip: (a) Is the onset of fracture determined by a critical stress state at the crack tip, independent of the crack size? (b) Why is K_c a material specific constant and what determines its magnitude? (c) Does the Rivlin–Thomas pure-shear protocol for elastomers [8] reveal similar physics to that involved in fracture of single-edge notched (SEN) specimens? (d) How does K_c depend on specimen thickness as plane stress changes to plane strain in the case of elastomers?

Because the stress buildup at the tip is found to saturate to a plateau, we are able to show given the spatial resolution of our *str*-POM method that (1) elastomeric fracture amounts to the stress at crack tip σ_{tip} reaching a threshold value $\sigma_{F(inh)}$ that may be identified as inherent strength, (2) σ_{tip} grows linearly with the nominal load σ, which appears in the stress intensity factor operationally defined as [4] $K = 1.12\sigma\sqrt{\pi a}$ for SEN, implying existence of a characteristic length scale P: $\sigma_{tip} = K/\sqrt{\mathrm{P}}$, (3) at fracture $K_c = \sigma_{F(inh)}\sqrt{\mathrm{P}}$, (4) in pure shear σ_{tip} also scales linearly with nominal load as $\sigma_{tip} = K_{ps}/\sqrt{\mathrm{P}}$, with $K_{ps} = \sigma\sqrt{h_0}$, where h_0 is the sample height h_0, (5) at fracture with SEN, the critical stress intensity factor $K_c = \sigma_{F(inh)}\sqrt{\mathrm{P}}$ is independent of the sample thickness D (ranging from 0.6 to 5 mm), with $\sigma_{F(inh)}$ decreasing with D and P increasing with D.

Given the *str*-POM observations, we *hypothesize* that elastomeric fracture may be understood to arise from the inherent strength $\sigma_{F(inh)}$ being exceeded at crack tip, and G_c is merely a measure of the energy release due to fracture. In other words, the tip stress $\sigma_{tip} \to \sigma_{F(inh)}$ corresponding to the load level $\sigma \to \sigma_c \sim \sigma_{F(inh)}\sqrt{\mathrm{P}/a}$, or $\sigma_{F(inh)}\sqrt{\mathrm{P}/h_0}$ in the respective cases of SEN and pure shear. This says that fracture occurs when the applied load σ reaches a fraction of $\sigma_{F(inh)}$ that is determined by the ratio P/a or P/h_0.

2. Results

2.1. Fracture of rubber sheets at different cut sizes (SEN)

Rivlin and Thomas has established [8] that for stretchable elastic bodies such as rubber fracture behavior can be characterized by measuring its toughness $G_{c(RT)}$ in terms of the work density of fracture w_c and cut size a [8,27,28]:

$$G_{c(RT)} = 6w(\lambda_c)a/\sqrt{\lambda_c}, \tag{1}$$

where λ_c is the critical stretching ratio at fracture of a precut specimen. This formulation derives from the Griffith style energy balance considerations. However, it was found since the beginning [8] that $G_{c(RT)}$ is orders of magnitude higher than surface fracture energy. This discrepancy has led researchers in the community to seek dissipative mechanisms [22] to account for the observed much greater energy release and to suggest that fracture at a finite speed cannot be idealized as involving only one monolayer of debonding, which is the case treated by the Lake and Thomas model [29] to describe the threshold for fatigue failure. For pure shear, Thomas also realized and demonstrated [30] that by preparing a precut of controlled radius $d/2$ for the tip, toughness can be found to scale approximately linearly with d.

By directly examining the stress buildup at crack tip in a precut BR specimen we explore the merit to adopt the Westergaard-Irwin's local stress approach [10,11] that recognizes $K = \sigma\sqrt{\pi a}$ as the loading parameter. Given the well-established stress optical relationship (SOR), shown in Fig. 1*A*, i.e., $\Delta n = C\sigma$, with $C = 2.92$ GPa^{-1}, we apply *str*-POM to quantify the stress field as a distance from the cut tip within a spatial resolution better than 10 μm. At $\theta = \pi/3$ to the crack propagation direction, the tensile stress field $T(r) = (\sigma_{yy} - \sigma_{xx})$ is also the principal stress difference, [26] thus linearly related to the birefringence Δn, i.e., $T = \Delta n(r)/C$, where C is the same stress-optical coefficient C, measured in Fig. 1*A*.

Quantitative spatial mapping of Δn shows in Fig. 1*B* that the stress field naturally saturates at the cut tip for four different cut sizes at various stages of tensile extension of the precut specimen, which is described in Supporting Information (SI.A). In such a plot, a Westergaard like solution describes the straight line in Fig. 1*B*, revealing

$$T = \sigma_{yy} - \sigma_{xx} = 0.69\sigma(a/r)^{1/2} \text{ for } r > r_{ss}. \tag{2}$$

Two comments are in order. First, stress saturation is observed under all eight conditions. This stress saturation zone (SSZ) emerges at a common distance r_{ss} from the tip, independent of cut size and load level, as indicated by values of 6, 10, 14 and 19 for $(a/r_{ss})^{1/2}$, corresponding to the respective values of a, so that r_{ss} = 20-22 μm under all conditions. To emphasize that the size of the SSZ is constant, we replot Fig. 1*B* to obtain Fig. 1*C*. While K varies from 0.28 to 0.51 MPa, r_{ss} remains approximately constant The SSZ is clearly not a plastic zone, having a fixed size instead of varying as K^2, i.e., by a factor of $(0.51/0.28)^2 = 3.3$. We have previously shown [26] that the emergence of SSZ is a result of a finite tip radius ρ_{tip}. In other words, r_{ss} is comparably determined by the natural tip blunting that occurs during precut making. Second, instead of locking onto a hypothetical σ_{YS}, the tip stress $\sigma_{tip} = T(r \to 0)$ increases linearly with K until the point of fracture. Consequently, the stress field T normalized by K collapses in Fig. 1*C*, apart from a small correction by the far-field load that manifests as a non-zero intercept on the ordinate.

The linear scaling relationship in Fig. 1*D* between σ_{tip} and K reveals [26] a characteristic length scale P that is constant at various stages of external loading including the onset of fracture, characterized by (K_c, $\sigma_{tip(F)}$). Thus, in terms of P, the critical stress intensity factor K_c acquires a new expression, besides its operational definition, given by

$$K_c = \sigma_c\sqrt{\pi a} = \sigma_{F(inh)}\sqrt{\mathrm{P}}, \tag{3}$$

where we suggest the tip stress at fracture as revealing inherent strength, i.e., $\sigma_{tip(F)} = \sigma_{F(inh)}$. Eq. (3) explains why K_c is material specific: Both $\sigma_{F(inh)}$ and P are material specific. The emergence of P originates from the existence of SSZ, which also persists during crack propagation as shown in Supporting Information (SI.A). It is instructive to note that the observation summarized by Eq. (3), i.e., $\sigma_{tip(F)} = \sigma_c\sqrt{\pi a/\mathrm{P}}$, is consistent with the Inglis solution, which shows the stress at a curved tip to be enhanced by a factor given by the square-root of the ratio of the crack size to tip radius. Indeed, P is related [26] to the tip radius ρ_{tip}.

Moreover, it is worth indicating that for the present BR samples the fracture toughness can be computed either from the operational definition of K_c for SEN or the Rivlin–Thomas formula Eq. (1). Table 1 shows the comparison between the two different estimates of G_c. They are clearly comparable. Finally, we note $\sigma_{tip(F)}$ read from Fig. 1*D* is lower than σ_b revealed in the inset of Fig. 1*A*. We interpret this difference to arise from the fact that fracture strength $\sigma_b \sim 5$ MPa is measured in uniaxial extension, i.e., in plane stress, whereas plane strain prevails at cut tip. We will continue the discussion in Section 3.1. Because of the stress triaxiality, the fracture can be expected to occur involving a lower level of birefringence. We examined a comparison between pure shear and uniaxial extension in Supporting Information to show that at a given extension the birefringence is lower in pure shear because of the additional dimensional constraint.

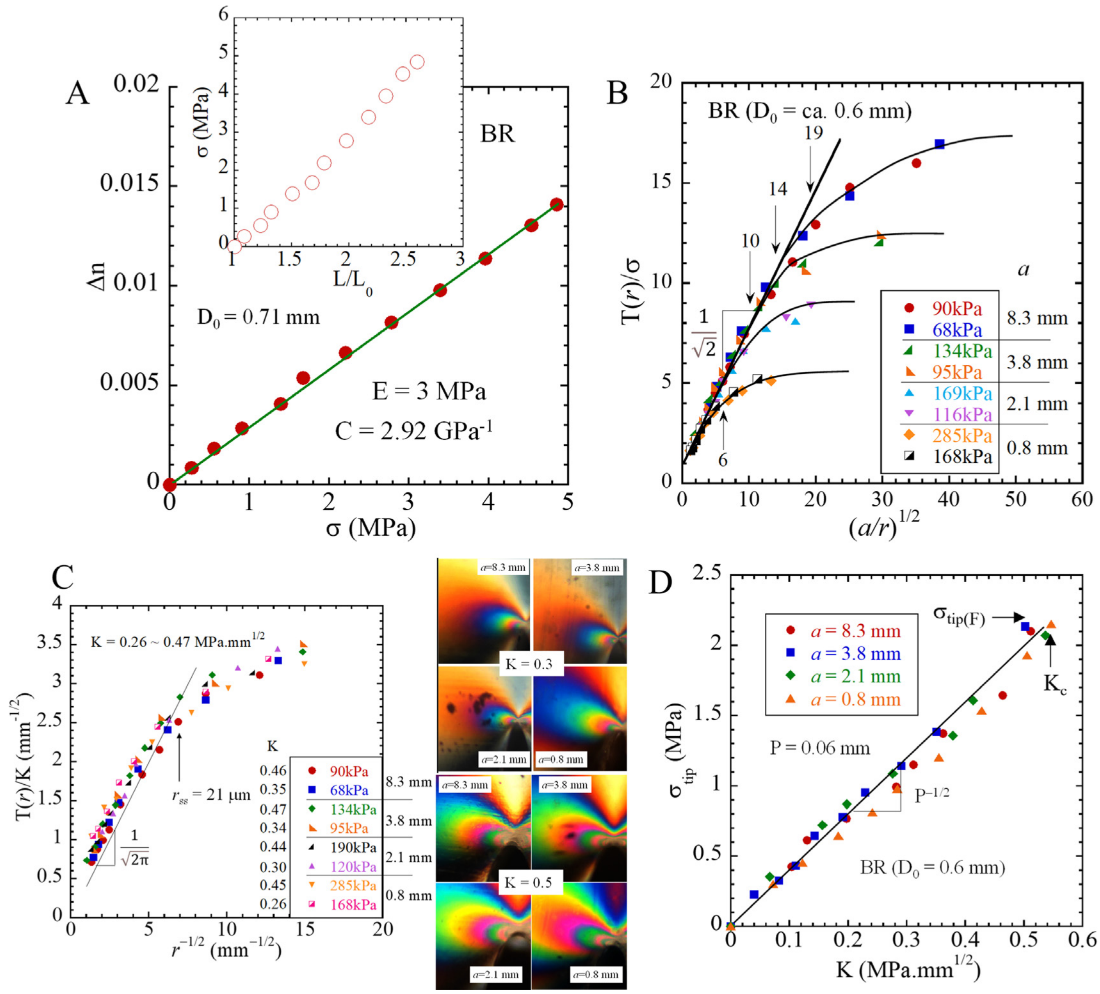

Fig. 1. (*A*) Stress optical relationship (SOR) through simultaneous mechanical and birefringence measurements of uncut BR specimen at $V/L = 0.05$ min^{-1}. The inset is the stress vs. strain curve of the specimen in terms of true stress σ and stretching ratio $\lambda = L/L_0$. (B) Normalized tensile stress field T/σ, read from SOR in (A) as a function $(a/r)^{1/2}$. Eq. (2), represented by the straight line, holds up to various values, i.e., 6, 10, 14 and 19 of $(a/r_{ss})^{1/2}$. For $r < r_{ss} = 21$ μm, T/σ saturates toward finite values. The curves are drawn to indicate the trend of stress saturation. (C) Various curves in (B) collapse when K instead of nominal load σ is used to normalize T, revealing a common r_{ss}, independent of K that ranges from 0.28 to 0.51 MPa mm$^{1/2}$. Two groups of images show the same birefringence level at the cut tip at $K = 0.3$ and 0.5 MPa mm$^{1/2}$. The different stages of stretching in (B) and (C) are labeled by the values of engineering stress. (D) Master curves of σ_{tip} vs. K for the four values of cut size a, revealing a linear scaling law, characterized by a new length scale P. The last points are the values of $K_c \sim 0.5$ MPa mm$^{1/2}$ and $\sigma_{F(inh)} \sim 2$ MPa at the onset of fracture.

Table 1
Toughness K_c and G_c of BR for different cut sizes[a].

Cut size a	Thickness D_0	ε_c	σ_c	$K_c = \sigma_c\sqrt{\pi a}$	$G_c = Kc^2/E$	$w(\lambda_c)$	$G_{c(RT)}$
8.4	0.62	0.037	0.100	0.51	87	1.8	89
3.8	0.61	0.059	0.148	0.51	87	4.4	97
2.1	0.55	0.075	0.209	0.54	105	7.1	95
0.8	0.61	0.137	0.347	0.55	101	23.0	100

[a]Lengths a and D_0 are in the unit of millimeters, $\varepsilon_c = \lambda_c - 1$, stress σ_c and modulus E in the unit of MPa, G_c and w_c are in the units of J/m^2 and kJ/m^3 respectively. Note that if we adopt (12) in Section 3 for K_c, G_c would be slightly higher than $G_{c(RT)}$.

2.2. Nature of fracture in pure shear

Rivlin and Thomas proposed an elegant protocol to account for the energy release during fracture of rubber. Specifically, the critical energy release rate was argued to show a simple form of $G_{ps(c)} = w_c h_0$ in the Rivlin–Thomas scenario, as shown in Supporting Information (SI.C). Since $G_{ps(c)}$ is usually constant, the Rivlin–Thomas expression explicitly suggests that a taller specimen with larger h_0 would undergo fracture at smaller strain because it has a larger volume and can store the same amount of energy at a lower energy density, i.e., $w_c = w(\lambda_c) \sim 1/h_0$: Larger h_0 corresponds to smaller λ_c. However, the results from the preceding II.A prompt us to look for a different interpretation of the Rivlin–Thomas formulation.

We proceed to examine three EPDM specimens of $h_0 = 18$, 48 and 120 mm in pure shear, where precut length c is half of the specimen width W of 100 mm. Here for pure shear c is used instead of a to denote the crack length. For pure shear, we adopt a different notation to denote cut length as c in place of a for SEN. The finding of preceding section informs us that fracture in pure shear would occur when the tip stress grows to reach $\sigma_{F(inh)}$. The characterization of pure shear fracture begins with

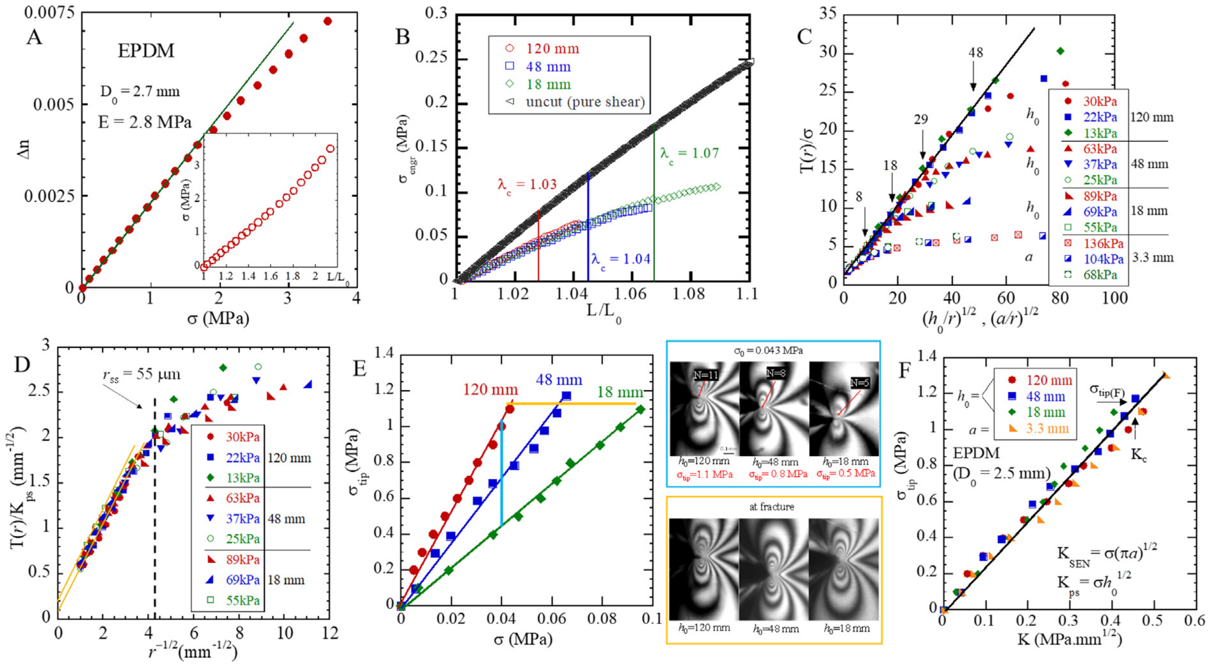

Fig. 2. (*A*) Stress optical relationship (SOR) through simultaneous mechanical and birefringence measurements of uncut EPDM specimen at $V/L = 0.05$ min^{-1}. The inset is the stress vs. strain curve of the specimen in terms of true stress σ and stretching ratio $\lambda = L/L_0$. (B) Engineering stress vs. nominal strain $\lambda = L/L_0$ of uncut (h_0, W = 100 mm) and precut (cut length $c = W/2 = 50$ mm) specimens of different heights $h_0 = 120$, 48 and 18 mm. (C) Normalized tensile stress field T/σ, at different values of σ read from SOR in (A) as a function $(h_0/r)^{1/2}$ or $(a/r)^{1/2}$, where the last group of data is a case of SEN with $a = 3.3$ mm. Eq. (5) represented by the straight line holds up to various values of $(a/r_{ss})^{1/2}$, i.e., 8, 18, 29 and 48 of $(h_0/r_{ss})^{1/2}$. For $r < r_{ss} = 55$ µm, T/σ saturates toward finite values. Here and in the subsequent (D), we label different stages of stretching with nominal stress, i.e., engineering stress. (D) Various curves in (C) collapse when K_{ps} of Eq. (4) is used to normalize T, revealing a common r_{ss}, independent of K_{ps}. The different stages of stretching in (C) and (D) are labeled by the values of engineering stress. (E) Tip stress (σ_{tip}) equal to T($r \to 0$) as a function of nominal load σ for $h_0 = 120$, 48 and 18 mm. The upper group of images depict the birefringence field near cut tip at a common load, indicated by the vertical (light blue, color online) line at 0.043 MPa; the lower group of images show the birefringence field at onset of fracture involving a common level of $\sigma_{tip(F)}$ around 1.14 MPa, indicated by the horizontal orange line. (F) Master curves of σ_{tip} vs. K for the three values of h_0, revealing a linear scaling law, involving a characteristic length scale P, the triangles denote the data from SEN. (For interpretation of the references to colour in this figure legend, the reader is referred to the web version of this article.)

experiments to determine the SOR for the EPDM specimens, from which the local stress field can be mapped out. Fig. 2*A* shows that the SOR is roughly a linear relation between tensile stress and birefringence. The slight deviation from the linearity might be due to the onset of non-Gaussian chain stretching. We show in Supporting Information (SI.B) that SOR can actually be applied to show a difference in the stress states between uniaxial extension and pure shear.

Fig. 2*B* Presents the relations between nominal load and nominal strain for both the uncut and precut specimens. Inspired by Fig. 1*B*, we make a similar observation as shown in Fig. 2*C* and reveal a similar feature that the local stress ceases to increases as $r^{-1/2}$ for $r < a = 3.3$ mm, where the stress field T(r) at $\theta = \pi/3$ is estimated using the stress-optical relationship from Fig. 2*A*. In place of the variable a, we have the specimen height h_0, which is the only pertinent length scale in the configuration [2]. According to the theoretical analysis in Supporting Information (SI.C), for linear elastic materials such as the present BR and EDPM samples with cut length c equal to *half* of specimen width W, we have the following expression for the load parameter K_{ps}.

$$K_{ps} = \sigma\sqrt{h_0} \tag{4}$$

in place of $K_{SEN} = \sigma\sqrt{\pi a}$. Like the Westergaard loading parameter K_{SEN} for SEN, we expect the pure shear to show stress intensification through K_{ps} as T(r) $\sim$ $K_{ps}/(2\pi r)^{1/2}$ at cut tip. Indeed Fig. 2*C* shows that away from the tip, T(r) scales as

$$T = 0.45\sigma(h_0/r)^{1/2} \text{ for } r > r_{ss}, \tag{5}$$

which is given by the straight line. In other words, all data involving three different values of h_0 fall on the same straight line until the emergence of SSZ in the same distance r from the cut tip, at $(h_0/r_{ss})^{1/2} = 18$, 29 and 50, i.e., at $r_{ss} = 0.055$ mm. This SSZ's size is independent of K_{ps}. Thus the SSZ has little to do with Irwin's plastic zone concept.

To emphasize the importance of the loading parameter K_{ps} whose operational definition is given in Eq. (4), similar to Fig. 1*C*, we can make Fig. 2*D* by normalizing the local tensile stress T with K_{ps} to illustrate analogous features. In the scaling regime, i.e., for $r > r_{ss}$, like Fig. 1*C*, the data show the same slope. However, they are not expected to collapse onto a single straight line because these lines have different intercepts given by $h_0^{-1/2}$ in Fig. 2*D* and by $a^{-1/2}$ in Fig. 1*C*.

The existence of SSZ allows the tip stress σ_{tip} to be measured as T($r = 0$) and expressed for all three values of h_0 as a function of load σ. Specifically, Fig. 2*E* shows how the tip stress varies with h_0 at various nominal loads. For example, at a common load of 0.043 MPa, indicated by the vertical line, at the time mark of ca. 72 s in the three videos in SI.F, σ_{tip} is higher for higher h_0. Reading Fig. 2*E* "horizontally", we see the same tip stress is reached at a lower load for higher h_0. The loading parameter K_{ps} of Eq. (4) can collapse the three lines in Fig. 2*E*, as shown by Fig. 2*F*.

Similar to Figs. 1*D*, 2*F* discloses a similar scaling law: $\sigma_{tip} = K_{ps}/\sqrt{\text{P}}$, obeyed by both pure shear and SEN data. The overlapping of the triangles with the other three sets of data confirms that Eq. (4) is the correct expression for K_{ps}. Fracture occurs in both SEN and pure shear at a comparable tip stress that is bounded by the inherent strength, with $K_{SEN(c)} \approx K_{ps(c)}$, which implies equivalently $G_{SEN(c)} \approx G_{ps(c)}$. In other words, similar to Eq. (3), we have

$$K_{ps(c)} = \sigma_c\sqrt{h_0} = \sigma_{F(inh)}\sqrt{\text{P}} \tag{6}$$

Table 2
Toughness K_c and G_c of EPDM: pure shear vs. SEN[a].

h_0 or a	Thickness D_0	ε_c	σ_c	K_c	$G_c = Kc^2/E$	$w(\lambda_c)$	$G_{c(RT)}$
120	2.50	0.026	0.043	0.47	80	1.1	66
48	2.56	0.043	0.066	0.46	74	2.7	65
18	2.51	0.064	0.095	0.40	58	6.1	55
3.3	2.49	0.075	0.163	0.53	99	5.7	106

[a]Lengths h_0, a and D_0 are in the unit of millimeters, $\varepsilon_c = \lambda_c - 1$, stress σ_c and modulus E in the unit of MPa, G_c and w are in the units of J/m^2 and kJ/m^3 respectively. K_c is evaluated from Eq. (4) for K_{ps} for the first three rows. K_c is the bottom row follows from $K_{SEN(c)} = \sigma_c\sqrt{\pi a}$ in MPa mm$^{1/2}$. $G_{c(RT)}$ is evaluated according to either Eq. (13) in Section 3.3 for pure shear or Eq. (1) for SEN.

Like K_c, σ_c acquires its meaning through either Eq. (6) for pure shear or Eq. (3) for SEN: it is given by $\sigma_{F(inh)}$ and the ratio of either h_0/P or a/P. Unlike K_c, σ_c is not a material constant because it depends on experimental parameters such as h_0 and a.

Since Fig. 2*C* reveals r_{ss} to be comparable in both pure shear and SEN, we expect the slope of the σ_{tip} vs. K to be comparable, i.e., involving a common P, leading to a collapse of the SEN data onto the master curve in Fig. 2*F*. Clearly, Eq. (4) is the correct formula for K_{ps} at $c = W/2$. On the other hand, K_c seems slightly higher in SEN than in pure shear. This leads to higher G_c for SEN as shown in Table 2 in comparison with pure shear. Also listed in Table 2 is $G_{c(RT)}$ given by either Eq. (1) for SEN and Eq. (13) for pure shear. The discrepancy of G_c between pure shear and SEN seem to arise from a difference in $\sigma_{F(inh)}$ that varies from SEN to pure shear. We return to this point in Section 3.1. Moreover, the relation between SEN and pure shear is further explored in Supporting Information (SI.D) based on a second rubber, i.e., BR.

2.3. Thickness dependence of toughness K_c: local characterization

2.3.1. Precut

If polymer fracture is dictated by crack tip reaching inherent strength, it is natural to ask whether and how inherent strength varies with the mode of deformation. Since the state of stress is known to change from plane stress to plane strain upon thickness increase, using BR with SEN, it is straightforward to find out how the critical condition for fracture depends on specimen thickness. Making precut of comparable size a around ca. 4.0 mm, Fig. 3*A* indicates that fracture occurs at a comparable K_c because the crack propagation occurs at a similar load level of $K_c = 0.49$ MPa mm$^{1/2}$, involving $\sigma_{engr} = 0.124$ MPa for $D_0 = 5.16$ mm and $a = 4.4$ mm and $\sigma_{engr} = 0.13$ MPa for $D_0 = 1.33$ mm and $a = 4.0$ mm as well as $\sigma_{engr} = 0.14$ MPa for $D_0 = 0.61$ and $a = 4.0$ mm.

We apply *str*-POM observation of the cut tip to show how K_c reaches a common level independent of thickness D_0. The data in Fig. 3*B* are unexpected, revealing not only emergence of SSZ, analogous to data in Figs. 1*C* and 2*D*, but also dependence of SSZ size r_{ss} on the specimen thickness D_0. Fig. 3*B* also suggests that at comparable loads (and a common nominal strain), e.g., common values of K, the tip stress σ_{tip} changes with D_0, lower for a larger D_0, as show in Fig. 3*C*, which also reveals three separate values for P, consistent with the fact that r_{ss} depends on D_0 (cf. Fig. 3*B*). The thickness effect can be more explicitly described in Fig. 3*D*: $\sigma_{tip(F)} = \sigma_{F(inh)}$ scales with D_0 to a negative power of 0.43 while $P^{1/2}$ roughly increases with D_0 in a power law with a positive exponent of 0.43 so that $K_c = \sigma_{F(inh)}P^{1/2}$ stays constant at 0.49 MPa mm$^{1/2}$.

We reiterate the explicit message revealed in Fig. 3*B*: At all values of K, the thicker specimen with $D_0 = 5.3$ avoids stress buildup by stress saturation at a greater distance from the crack tip. To further characterize the thickness effect, local thickness at the cup tip is measured during stretching in separate tests. Fig. 3*E* shows that the local thickness at the tip decreases with nominal strain L/L$_0$, going faster for the thinner specimen. The greater thickness change at the tip amounts to greater stress buildup. In other words, the thicker specimen has greater capacity to avoid the buildup at the tip. Fig. 3*F* indicates that the higher tip stress is actually associated with the greater thickness change at the tip.

Table 3
Fracture of BR under preload.

0.2 MPa			
D_0 (mm)	0.68	1.37	5.40
a_c (mm)	2.87	3.48	2.97
K_c (MPa mm$^{1/2}$)	0.65	0.71	0.67
0.15 MPa			
D_0 (mm)	0.53	1.43	5.27
a_c (mm)	4.92	5.17	5.23
K_c (MPa mm$^{1/2}$)	0.62	0.64	0.65
0.12 MPa			
D_0 (mm)	0.63	1.44	5.31
a_c (mm)	5.92	6.37	6.71
K_c (MPa mm$^{1/2}$)	0.54	0.56	0.58

2.3.2. Preload

As stated in the beginning of Section 2.3.1, catastrophic fracture occurs at comparable nominal loads or common K_c as indicated by Figs. 3*A*, 3*C* and 3*D*. To confirm that the critical condition for fracture is indeed independent of thickness, we pre-load uncut BR specimens to different levels and then force a blade from one edge into the specimen to produce a crack of increasing length until catastrophic fracture at a critical cut size a_c. Specifically, we discretely preload BR specimens to three levels of σ_{engr} = 0.12, 0.15 and 0.20 MPa for each of the three thicknesses using a constant load mode. As shown in Table 3, for three preloads of 0.2, 0.15 and 0.12 MPa, the blade advances to three different sets of distances before spontaneous fracture, revealing a similar cut size for a given preload, roughly independent of D_0. Here the values of a_c can be readily measured from the fractured specimens since the catastrophic fracture produces much rougher surfaces relative to that made by the blade, as shown by images of fracture surface in Supporting Information (SI.E). The duration of blade advancement is characterized by Instron measurement of clamp movements, also presented in Supporting Information (SI.E). With increasing load σ, a_c decreases, leading to a constant $K_c = \sigma\sqrt{\pi a_c}$. Specifically, Table 3 lists the values of K_c that are roughly thickness independent, showing slight increase with the load σ, ranging from 0.71 MPa mm$^{1/2}$ for $\sigma_{engr} = 0.2$ MPa to 0.56 MPa mm$^{1/2}$ for $\sigma_{engr} = 0.12$ MPa, which is comparable to the level obtained from precut specimens (cf. Table 1). In other words, these preload tests confirm that the toughness is indeed constant independent of the specimen thickness.

3. Discussion

3.1. Inherent strength $\sigma_{F(inh)}$

We have defined the tip stress at fracture as inherent strength $\sigma_{F(inh)}$. The *str*-POM observations in Section 2.3.1 indicate that

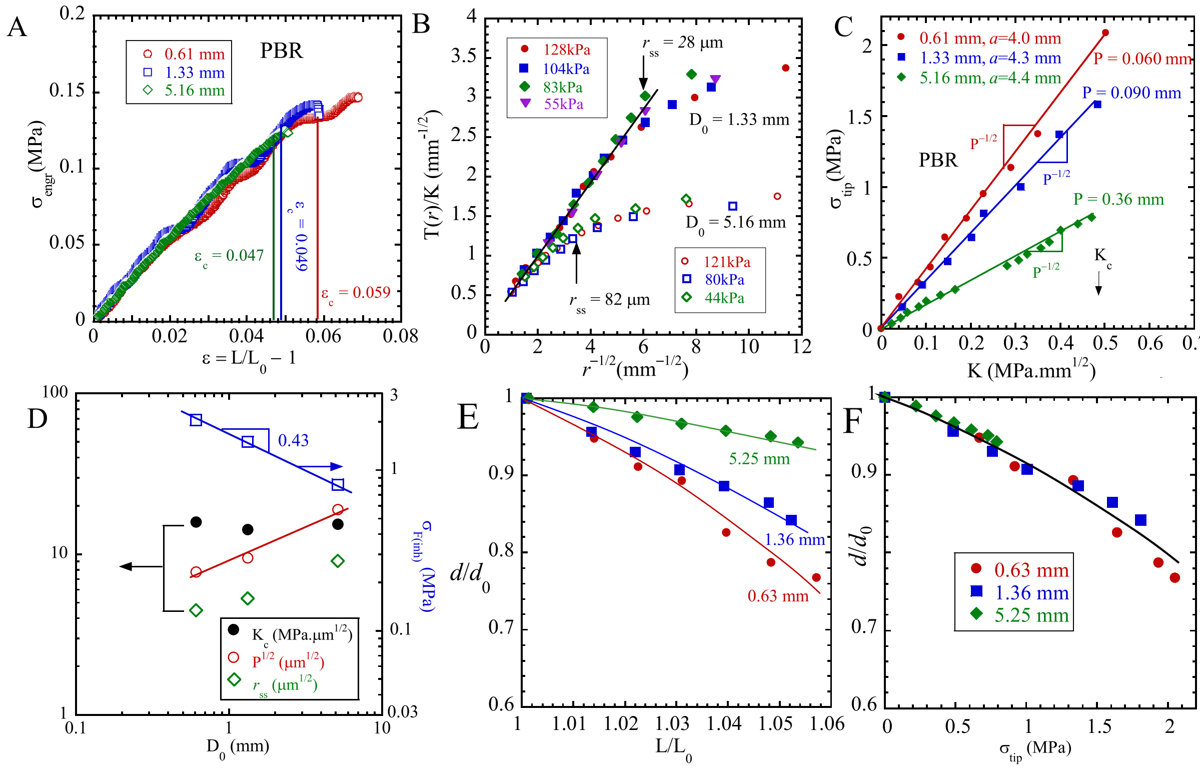

Fig. 3. (*A*) Engineering stress vs. nominal strain $\varepsilon = L/L_0 - 1$ of precut BR specimens of different $D_0 = 0.61$, 1.33 and 5.16 mm. (B) Normalized tensile stress field T/K at various nominal load $\sigma = 55$, 83, 104 and 128 kPa as a function of $r^{-1/2}$ for $D_0 = 1.33$ and 5.16 mm. (C) Tip stress σ_{tip} vs. K, showing different slopes and thus revealing different P values at different values of D_0 yet a common K_c. (D) SSZ size r_{ss} and corresponding P as well as $\sigma_{F(inh)}$ as a function of specimen thickness D_0. The opposing scaling of P and $\sigma_{F(inh)}$ leads to independence of K_c on D_0, denoted by filled circles. (E) Local thickness decreases at cut tip during extension, i.e., as a function of nominal draw ratio L/L_0. (F) Master curve of d/d_0 against the tip stress σ_{tip}, with the smooth curve as guide for the eye.

$\sigma_{F(inh)}$ is not constant and varies with specimen thickness. The origin of this variation remains elusive. On the other hand, it is clear that $\sigma_{F(inh)}$ is appreciably lower than the fracture strength (i.e., breaking stress) of uncut specimen, denoted by σ_b. To understand this difference, it is helpful to note that the uniaxial extension (along Y axis) is described by a single non-zero component σ_{yy} with $\sigma_{xx} = \sigma_{zz} = 0$, which can be quantified through SOR as

$$\sigma_{yy} = \sigma_{yy} - \sigma_{xx} = \Delta\sigma = \Delta n/C. \tag{7}$$

In contrast, according to the Westergaard description of the stress field near the tip, at $\theta = \pi/3$, $\sigma_{yy} = 3\sigma_{xx}$ so that the SOR amounts to

$$\sigma_{yy} = (3/2)\Delta n/C, \tag{8}$$

$$\sigma_{xx} = \sigma_{yy}/3 = (1/2)\Delta n/C, \tag{9}$$

and

$$\sigma_{tip} = T(r \to 0, \theta = \pi/3) = \Delta n(r \to 0)/C, \tag{10}$$

which is lower than σ_{yy} by a factor of 2/3. We expect *str*-POM observations to reveal

$$(3/2)\sigma_{F(inh)} < \sigma_b \tag{11}$$

because fracture occurs at σ_b under unconstrained condition of $\sigma_{xx} = \sigma_{zz} = 0$ while fracture at the tip occurs under severe constraint of $\sigma_{xx} = \sigma_{yy}/3$ and σ_{zz} ranging from 0 to $2\sigma_{xx}$ (with Poisson ratio $\nu = \frac{1}{2}$). To clarify, Eq. (11) supports our assertion that elastomeric fracture under constraint (i.e., with $\sigma_{xx} > 0$ and $\sigma_{zz} \geq 0$) would occur at lower σ_{yy} than σ_b measured from the uniaxial extension of uncut specimen. While a chain-level theory of inherent strength for elastomers under different deformation modes is non-existent, the preceding assertion is self-evident.

It is necessary to further recognize that the value of $\sigma_{F(inh)}$ (relative to σ_b, which we regard as inherent strength for uniaxial stretching) may also depend on whether σ_{zz} is zero or finite. For example, apparently, the specimen thickness regulates the stress state at cut tip, causing $\sigma_{F(inh)}$ to vary, as implied by the data in Section 2.3.1. Moreover, the difference found in K_c between SEN and pure shear, as listed in Table 2, may also indicate a notable difference in $\sigma_{F(inh)}$. It is plausible that the mode of global extension, e.g., uniaxial vs. pure shear, can influence the state of deformation at the cut tip, leading to differences in $\sigma_{F(inh)}$.

3.2. Single-edge notch (SEN)

For rubber such as the present BR and EPDM, the stress buildup is found to saturate so that it is feasible to characterize the tip stress σ_{tip} as a function of the nominal load σ or stress intensity factor K based on its operational definition. The stress buildup at the cut tip is prescribed by the combination of nominal load σ and cut size a, as anticipated by linear elastic fracture mechanics. Indeed, fracture from precut specimen is a local event, dependent on the stress intensification at the cut tip and independent of global configurations such as the variation from SEN to pure shear. For SEN, the tensile stress field T at a distance r from the tip and angle $\theta = \pi/3$, after normalization by the nominal load σ, can be expected [26], according to the Westergaard solution [10], as

$$T/\sigma = 1.12\sin(\pi/3)\left(K_{exp}/K_{theor}\right)\sqrt{a/2r} + 1, \tag{12}$$

with the theoretical operational definition [4]

$$K_{theor} = 1.12\sigma\sqrt{\pi a}. \tag{13}$$

Unity in Eq. (12) denotes the fact that the far-field stress is comparable to the nominal load. Comparing Eq. (12) with the experimental result described by Eq. (2), we have $K_{exp} = K_{theor}$.

3.3. Pure shear

For pure shear, analogous to Eq. (1), Rivlin and Thomas proposed the following widely used expression for $G_{ps(c)}$ as

$$G_{ps(c)} = w(\lambda_c)h_0/2, \tag{14}$$

which is re-drived in Supporting Information (SI.C). Parallel to the case of SEN, we can envision stress intensification in pure shear to be characterized by a stress intensity factor K_{ps}, involving an expression similar to Eq. (12). The exact form of K_{ps} given in Eq. (4) is derived in the Supporting Information (SI.C). Specifically, because of the scaling form in Eq. (4), the following expression can be expected in the K_{ps} annulus for the local stress field driven by the nominal load σ

$$T/\sigma = B\sqrt{h_0/r} + 2, \text{ at } \theta = \pi/3, \tag{15}$$

where the factor of two arises from the special case of the cut length c in pure shear equal to half width, W/2, so that the nominal load σ is half of the far-field stress σ_{uc} equal to that of uncut specimen. Eq. (15) suggests that the pure shear data should be analyzed by plotting T/σ against normalized distance $\sqrt{h_0/r}$ for different values of h_0. This is indeed the case according to the experimental data in Fig. 2*C*, partically described by Eq. (5), showing $B = 0.45$.

Rivlin–Thomas [8] varied h_0 by a factor of three to validate Eq. (14) that G_c is a material constant, independent of h_0, i.e., $w_c \sim 1/h_0$. The form of Eq. (14) conveys the message that the energy balance argument is valid: The taller specimen has more volume to store energy and thus only needs to involve a lower level of strain energy to produce the same energy release rate. In their subsequent papers from II to XI, Rivlin and Thomas did not return to the question of whether and why Eq. (14) holds for different values of h_0. Soon after their Paper I Thomas became aware [30] that G_c may be related to the strain distribution around a blunted crack tip. Unfortunately, Thomas did not proceed to show that Eq. (14) may have its origin in the local stress intensification that increases with h_0, as shown by Eqs. (4) and (15): At a given nominal strain λ, the local stress field near crack tip is higher at a larger h_0.

Str-POM observation of the stress field near crack tip unravels the hidden meaning of Eq. (14). In other words, we explain for the first time why $w_c \sim 1/h_0$, as implied by Eq. (14). We show by the specific experiments elaborated in Section 2.2 that K_{ps} of Eq. (4) indeed holds, i.e., the tip stress actually builds up in linear proportion to $K_{ps} \sim \sqrt{h_0}$, or more generally Eq. (15) holds true. To our knowledge, there is no theoretical derivation of Eq. (15) for linear elastic materials in pure shear configuration. We have established this relation by experiment and elucidated the actual meaning of the Rivlin–Thomas formula, Eq. (14). In other words, $G \to G_{ps(c)}$ reflects a stress criterion, showing the consequence of $\sigma_{tip} \to \sigma_{F(inh)}$, which is universal, e.g., is also the fracture criterion for SEN configuration.

Thanks to Irwin's demonstration [11,31] to show $G = K^2/$ E, where K is Irwin's stress intensity factor and E the Young's modulus, we can arrive at an expression for toughness G_c as

$$G_c = Kc^2/E = (\sigma_c^2/E)h_0 = 2w_F P, \text{ with } w_F = (\sigma_{F(inh)})^2/2E, \tag{16}$$

where w_F is the work of fracture. Thus, Eq. (16) shows that P prescribes the value for the fracto-cohesive length [32] $L_{fc} = Gc/w_F$ and is the origin of this length scale. In other words, since P originates from the finite tip radius $d/2$, the origin of L_{fc} is the natural tip blunting. Moreover, Eq. (16) is consistent with Thomas' approximate demonstration [30] that G_c linearly depends on tip diameter d. We note that the same expression applies to SEN. Thus, Eqs. (3) and (16) describe the actual meaning of toughness K_c and G_c, with G_c computable from K_c.

3.4. Generic expression for G_c

Eq. (16) actually holds universally as an expression for G_c and can be argued to be true at the scaling level by considering the majority of energy storage per unit fracture surface. When the crack advances by δ in the specimen of thickness D, involving an area of $\Delta A = D\delta$, the energy release is controlled by $\sigma_{F(inh)}$ in SSZ of size P, given by $\Delta U = (\sigma^2_{F(inh)}/2E)(2PD\delta)$ so that $G_c = \Delta U/\Delta A = 2w_F P$, which is Eq. (16).

4. Conclusion

Spatial–temporal resolved POM (*str*-POM) observations show that the stress buildup at crack tip saturates at all levels of applied load at a sizable distance (beyond 20 μm) from crack tip. Existence of a stress saturation zone (SSZ) permits tip stress σ_{tip} to be determined as a function of nominal load or stress intensity factor K (through its operational definition). The observed linear growth of σ_{tip} with K arises from the existence of a finite tip radius. Moreover, this linear scaling reveals a new characteristic length scale $P = (K/\sigma_{tip})^2$. Since the size of SSZ is independent of K, SSZ cannot regarded as an Irwin process zone. On the other hand, sizable process zone has been reported for toughened elastomers [33–35]. Separately, theoretical studies have suggested [36–39] that the local stress can saturate upon approaching the tip due to the finite curvature of crack tip.

Based on three independent sets of *str*-POM studies, we show that elastomeric fracture may be characterized in terms of a stress-based criterion rather than Griffith energy-balance argument. Independent of geometric configuration, e.g., for different cut sizes in single-edge notch, different specimen thicknesses, pure shear (planar extension) vs. uniaxial extension, the onset of fracture is shown to be governed by the criterion of tip stress reaching a threshold level, designated as inherent strength. This stress criterion allows us to explain how the LEFM phenomenology emerges in reality. For example, Eq. (3) explicitly shows (a) why K_c is a material constant — because both inherent strength $\sigma_{F(inh)}$ and P are material specific, and (b) a combination inherent strength $\sigma_{F(inh)}$ and P determine the magnitude of K_c and $G_c = K_c^2/E$, per Eqs. (3) and (16) respectively.

The *str*-POM observation of stress buildup at crack tip suggests that the widely used pure shear protocol of Rivlin and Thomas [8] to characterize toughness of elastomers has its origin in the tip stress scaling with specimen height h_0 as $\sigma_{tip} \sim K_{ps} = \sigma\sqrt{h_0}$. In other words, we have uncovered the meaning of Rivlin–Thomas Eq. (14) that stress intensification depends on h_0 and fracture is tip stress controlled.

Finally, through *str*-POM, we are now able to show how elastomeric fracture occurs at a common K_c, independent of specimen thickness D_0, [16] unlike the case of plastics [15]. Specifically, the local deformation at crack tip varies with D_0, showing stress saturation at a larger distance from the tip for a thicker specimen, corresponding to weaker deformation at the tip, with fracture observed to commence at a lower tip stress, i.e., lower inherent strength.

Materials and methods

Materials and Sample Preparation

Polybutadiene rubber (BR) from The Goodyear Tire & Rubber Company (BUD1207) and ethylene propylene diene monomer

(EPDM) from Lion Elastomers (Royalene 511) were studied in this work. Only dicumyl peroxide is added as the crosslinking agent to guarantee transparency in BR. BR sheets with thickness 0.6–5.3 mm were cured by heat compression molding with 1 phr dicumyl peroxide (Acros Organics) at 160 °C for 60 min. EPDM sheets with thickness 2–2.5 mm were prepared by Gregory Brust at Lion Elastomers using tri-functional crosslinker SR-350 (1∼3 phr), and peroxide DiCup R (3∼4 phr), at 170 °C for 20 min.

Dogbones were cut using type V die (ASTM D638). They are used to establish the stress-optical relationship. Strip-shaped specimens were cut into desired dimensions by a paper cutter. Precut specimens involving edge notch, i.e., either single-edge notch (SEN) or pure shear with cut length being half of the specimen width, are made by gently pushing a razor blade (Feather Safety Razor Co., Ltd.) into specimens. The cut size to width ratio (a/W) for all SEN is kept smaller than 0.2. For cut sizes smaller than ca. 4 mm, the length and width of the specimen is chosen to be 50 × 20 mm^2; for cut sizes larger than 4 mm, length and width is chosen to be 80 × 40 mm^2.

Methods

Tensile experiments were carried out on an Instron 5543 tensile tester at room temperature. Photoelastic characteristics of BR and EPDM were mapped both spatially and temporally around the cut tip using a *str*-POM setup [26] described in a previous study. To capture the development of birefringence during stretching, video camera (Mokose C100) with 4K resolution was used along with two different magnification-adjustable micro-lenses (Edmund Industrial Optics (EIO) and Hayear model HY-180XA). The *str*-POM observations in Section 2.1 involved 8× magnification on EIO. For data in Section 2.2, Hayear lens at 2.25× was used. Finally, for *str*-POM observations presented in Section 2.3, magnification on EIO was set at 7×, 5× and 2.5×, corresponding to $D_0 = 0.61$, 1.33 and 5.16 mm respectively.

The monochromatic light source for most of our *str*-POM observations is a low-pressure sodium lamp (Phillips). For samples with thickness less than 0.7 mm, we adopt white light and use Michel-Levy charter to make more accurate measurements of birefringence. For preload tests presented in II.C.2, the same razor blade is advanced into one of the two edges of a strip-shaped specimen until the point of fracture.

CRediT authorship contribution statement

Zehao Fan: Development of quantitative birefringence measurements, Data curation, Formal analysis, Validation, Writing – materials and methods section. **Shi-Qing Wang:** Supervision, Conceptualization, Methodology, Formal analysis, Validation, Writing – original draft, Writing – review & editing.

Declaration of competing interest

The authors declare that they have no known competing financial interests or personal relationships that could have appeared to influence the work reported in this paper.

Data availability

Data will be made available on request.

Acknowledgments

This work is supported, in part, by the Polymers program at the USA National Science Foundation (DMR-1905870, 2210184). SQW would like to thank Dr. Zhigang Suo for a conversation on the manuscript who emphasized $G \to G_c$ is a fracture criterion although it does not describe a fracture mechanism. We are grateful to Dr. Gregory Brust at Lion Elastomers for providing us with the EPDM sheets.

Appendix A. Supplementary data

Supplementary material related to this article can be found online at https://doi.org/10.1016/j.eml.2023.101986.

References

[1] C. Creton, M. Ciccotti, Fracture and adhesion of soft materials: a review, Rep. Progr. Phys. 79 (4) (2016).
[2] R. Long, C.-Y. Hui, J.P. Gong, E. Bouchbinder, The fracture of highly deformable soft materials: A tale of two length scales, Annu. Rev. Condens. Matter Phys. 12 (2021) 71–94.
[3] A.A. Griffith, VI The phenomena of rupture and flow in solids, in: Philosophical Transactions of the Royal Society of London, in: Series A, containing papers of a mathematical or physical character, vol. 221, (582–593) 1921, pp. 163–198.
[4] T.L. Anderson, Fracture Mechanics: Fundamentals and Applications, CRC Press, 2017.
[5] A.J. Kinloch, Fracture Behaviour of Polymers, Springer Science & Business Media, 2013.
[6] J. Berry, Fracture processes in polymeric materials. I. The surface energy of poly (methyl methacrylate), J. Polym. Sci. 50 (153) (1961) 107–115.
[7] J. Berry, Fracture processes in polymeric materials. II. The tensile strength of polystyrene, J. Polym. Sci. 50 (154) (1961) 313–321.
[8] R. Rivlin, A.G. Thomas, Rupture of rubber. I. Characteristic energy for tearing, J. Polym. Sci. 10 (3) (1953) 291–318.
[9] C.E. Inglis, Stresses in a plate due to the presence of cracks and sharp corners, Trans. Inst. Naval Archit. 55 (1913) 219–241.
[10] H.M. Westergaard, Bearing pressures and cracks, Trans. AIME, J. Appl. Mech. 6 (1939) 49–53.
[11] G.R. Irwin, Analysis of stresses and strains near the end of a crack transversing a plate, Trans. ASME, Ser. E, J. Appl. Mech. 24 (1957) 361–364.
[12] C.-T. Sun, Z. Jin, Fracture Mechanics, Academic Press, 2011.
[13] M.L. Williams, On the stress distribution at the base of a stationary crack, J. Appl. Mech. 24 (1957) 109–114.
[14] G.R. Irwin, Onset of fast crack propagation in high strength steel and aluminum alloys, in: Sagamore Research Conference Proceedings, 1956, pp 289–305.
[15] R.A.W. Fraser, I.M. Ward, Temperature dependence of craze shape and fracture in polycarbonate, Polymer 19 (2) (1978) 220–224.
[16] G.J. Lake, High-speed fracture of elastomers: Part I, Rubber Chem. Technol. 73 (5) (2000) 801–817.
[17] A.K.A.G. Thomas, Tear behavior of rubbers over a wide range of rates, Rubber Chem. Technol. 54 (1) (1981) 15–23.
[18] Gent A., S. Lai, C. Nah, C. Wang, Viscoelastic effects in cutting and tearing rubber, Rubber Chem. Technol. 67 (4) (1994) 610–618.
[19] A. Gent, Adhesion and strength of viscoelastic solids. Is there a relationship between adhesion and bulk properties? Langmuir 12 (19) (1996) 4492–4496.
[20] P. De Gennes, Weak adhesive junctions, J. Physique 50 (18) (1989) 2551–2562.
[21] P.-G. de Gennes, Soft adhesives, Langmuir 12 (19) (1996) 4497–4500.
[22] C. Creton, 50Th anniversary perspective: Networks and gels: Soft but dynamic and tough, Macromolecules 50 (21) (2017) 8297–8316.
[23] B. Persson, E. Brener, Crack propagation in viscoelastic solids, Phys. Rev. E 71 (3) (2005) 036123.
[24] L. Mullins, Rupture of rubber. IX. Role of hysteresis in the tearing of rubber, Trans. Inst. Rubber Ind. 35 (5) (1958) 213–222.
[25] H. Greensmith, L. Mullins, A. Thomas, Rupture of rubber, Trans. Soc. Rheol. 4 (1) (1960) 179–189.
[26] T. Smith, C. Gupta, Z. Fan, G.J. Brust, R. Vogelsong, C. Carr, S.-Q. Wang, Toughness arising from inherent strength of polymers, Extreme Mech. Lett. (2022) 101819.
[27] H. Greensmith, Rupture of rubber. X. The change in stored energy on making a small cut in a test piece held in simple extension, J. Appl. Polym. Sci. 7 (3) (1963) 993–1002.
[28] C. Creton, M. Ciccotti, Fracture and adhesion of soft materials: a review, Rep. Progr. Phys. 79 (4) (2016) 046601.
[29] G. Lake, A. Thomas, The strength of highly elastic materials, Proc. R. Soc. Lond. Ser. A Math. Phys. Eng. Sci. 300 (1460) (1967) 108–119.
[30] A. Thomas, Rupture of rubber. II. The strain concentration at an incision, J. Polym. Sci. 18 (1955) 177–188.
[31] G. Irwin, Relation of stresses near a crack to the crack extension force, in: 9th Cong. App. Mech., Brussels, 1957.
[32] C. Yang, T. Yin, Z. Suo, Polyacrylamide hydrogels. I. Network imperfection, J. Mech. Phys. Solids 131 (2019) 43–55.
[33] E. Ducrot, Y.L. Chen, M. Bulters, R.P. Sijbesma, C. Creton, Toughening elastomers with sacrificial bonds and watching them break, Science 344 (6180) (2014) 186–189.

[34] J. Slootman, V. Waltz, C.J. Yeh, C. Baumann, R. Göstl, J. Comtet, C. Creton, Quantifying rate-and temperature-dependent molecular damage in elastomer fracture, Phys. Rev. X 10 (4) (2020) 041045.
[35] Y. Chen, C.J. Yeh, Y. Qi, R. Long, C. Creton, From force-responsive molecules to quantifying and mapping stresses in soft materials, Sci. Adv. 6 (20) (2020) eaaz5093.
[36] G. Glinka, Calculation of inelastic notch-tip strain-stress histories under cyclic loading, Eng. Fract. Mech. 22 (5) (1985) 839–854.
[37] G. Glinka, A. Newport, Universal features of elastic notch-tip stress fields, Int. J. Fatigue 9 (3) (1987) 143–150.
[38] P. Lazzarin, R. Tovo, A unified approach to the evaluation of linear elastic stress fields in the neighborhood of cracks and notches, Int. J. Fract. 78 (1) (1996) 3–19.
[39] S. Filippi, P. Lazzarin, R. Tovo, Developments of some explicit formulas useful to describe elastic stress fields ahead of notches in plates, Int. J. Solids Struct. 39 (17) (2002) 4543–4565.